Hollow magnetic-fluorescent nanoparticles for dual-modality virus detection

Hollow magnetic-fluorescent nanoparticles for dual-modality virus detection

Akhilesh Babu Ganganboina,[1] Ankan Dutta Chowdhury,[1] Indra Memdi Khoris,[2] Ruey-an Doong,[3] Tian-Cheng Li,[4] Toshimi Hara,[5] Fuyuki Abe,[5] Tetsuro Suzuki,[6] Enoch Y. Park[1,2,*]

[1] Research Institute of Green Science and Technology, Shizuoka University, 836 Ohya Suruga-ku, Shizuoka 422-8529, Japan

[2] Department of Bioscience, Graduate School of Science and Technology, Shizuoka University, 836 Ohya Suruga-ku, Shizuoka 422-8529, Japan

[3] Institute of Analytical and Environmental Sciences, 101, Section 2, Kuang-Fu Road, National Tsing Hua University, Hsinchu 30013, Taiwan

[4] Department of Virology 2, National Institute of Infectious Diseases, 4-7-1 Gakuen, Musashimurayam-shi, Tokyo 208-0011, Japan

[5] Department of Microbiology, Shizuoka Institute of Environment and Hygiene, 4-27-2, Kita-ando, Aoi-ku, Shizuoka 420-8637, Japan

[6] Department of Infectious Diseases, Hamamatsu University School of Medicine, 1-20-1 Higashi-ku, Handa-yama, Hamamatsu 431-3192, Japan

E-mail addresses:
akhilesh.babu.ganganboina@shizuoka.ac.jp (ABG)
ankan.dutta.chowdhury@shizuoka.ac.jp (ADC)
Indra.memdi.khoris.17@shizuoka.ac.jp (IMK)
radoong@mx.nthu.edu.tw (RAD)
litc@nih.go.jp (TCL)
toshimi1_hara@pref.shizuoka.lg.jp (TH)
fuyuki1_abe@pref.shizuoka.lg.jp (FA)
tesuzuki@hama-med.ac.jp (TS)
park.enoch@shizuoka.ac.jp (EYP)

[*] Corresponding author at: Research Institute of Green Science and Technology, Shizuoka University, 836 Ohya, Suruga-ku, Shizuoka 422-8529, Japan.
E-mail address: park.enoch@shizuoka.ac.jp (E.Y. Park). Tel (Fax): +81-54-238-4887)

Abstract

Combination of magnetic nanomaterials with multifunctionality is an emerging class of materials that exhibit tremendous potential in advanced applications. Synthesizing such novel nanocomposites without compromising magnetic behavior and introducing added functional properties is proven challenging. In this study, an optically active quantum dot (QD) (core) encapsulated inside iron oxide (hollow shell) is prepared as the first electrochemical/fluorescence dual-modality probe. Presence of magnetic layer on the surface enables excellent magnetic property and the encapsulating of QDs on the hollow shell structure maintains the fluorescence with minimal quenching effect, endowing for potential application with fluorescence modality readout. We successfully demonstrate dual-modality sensing utilizing of QD-encapsulated magnetic hollow sphere nanoparticles (QD@MHS NPs) with magnetic separation ability and highly integrated multimodal sensing for the detection of various viruses including hepatitis E virus (HEV), HEV-like particles (HEV-LPs), norovirus-like particles (NoV-LPs), and norovirus (NoV) from clinical specimens. Most importantly, fecal samples of HEV-infected monkey are successfully diagnosed with sensitivity similar to gold standard real-time quantitative reverse transcription-polymerase chain reaction (RT-qPCR). This well-defined QD@MHS NPs-based nanoplatform intelligently integrates dual-modality sensing and magnetic bio-separation, which open a gateway to provide an efficient point-of care testing for virus diagnostics.

Keywords: Multicomponent nanoparticles; Fluorescence; Impedance; Dual-modality; Bio-separation; Virus diagnostics.

1. Introduction

The design and fabrication of multicomponent effective nanoparticles with unique properties that arise from mutual interactions among the individual constituents is a central goal of diagnosis-oriented nanotechnology advancement (Alivisatos 2004; Juárez et al., 2007; Milliron et al., 2004). Every sensing method has its own drawbacks, combining different methods into multimodal sensing can provide complementary information (Chuong et al., 2017; Park et al., 2020; Wu et al., 2019). Fabrication of nanomaterials with more than one functional constituent, which act as bifunctional markers, is fascinating.

Magnetic nanoparticles rapidly separate and enrich samples from a complex matrix and have been utilized for considerable improvement of the sensitivity and reducing the interference from other materials (Li et al., 2016a; Oh et al., 2018). Combining the magnetic nanoparticles with other functional components will help to achieve hybrid nanomaterials that exhibit various properties synergistically. The inorganic fluorescent quantum dots (QDs) with strong fluorescence intensity are an attractive component and are broadly adopted for high-throughput detection (Shrivastava et al., 2020), Magneto-fluorescent nanoparticles with magnetic and fluorescence have been recognized as an emerging class of materials with diverse potential in bio-separation and detection (Bruns et al., 2009; Chen et al., 2014). Co-encapsulation into inorganic materials like silica, template-based syntheses using physical appendage or chemical bonding, or attachment of separate nanoparticles are majorly used synthesis strategies of magneto-fluorescent materials (Cho et al., 2014; Kim et al., 2006; Lee et al., 2015). Precautions must be taken to reduce the unnecessary interactions within the nanocomposite that might deteriorate the optical or magnetic properties (Chen et al. 2014; Shevchenko et al., 2008). Several reports show that contact among the QDs and magnetic particles can reduce the desired optical properties (Boldt et al., 2011; Feld et al., 2015), This can be reduced or avoided predominantly if an effective separation layer between two

nanomaterials can be achieved. Chen et al. (2014) prepared colloidal structures by co-assembling magnetic nanoparticles (core) with fluorescent QDs (shell) surrounded by a thin layer of silica. These nano-assemblies exhibit high magnetic content and fluorophore loading. Although developing nanohybrids combining the magnetic and fluorescent particles are successful, the inside core creates significant influence on the fluorescence properties and size of the nanoparticles may be big because of assembling several magnetic and fluorometric nanoparticles. It indicates that rather than combining both magnetic and fluorescent components into an insulating matrix, both should combine into a single entity with unique morphology.

Multifunctional nanomaterials enhance the diversity of sensing and also enrich the possibility of transformation from a single-modality assay to a dual-modality assay (Chen et al., 2019; Dang et al., 2020; Ganganboina and Doong 2018; Ganganboina et al., 2018; Ganganboina et al., 2020). Dual or multi-modality sensors are the collaborative association of two or more detection methods, enabled by single or multimodal probes which ensure enhanced detection sensitivity and better reliability of collected data (Xiong et al., 2018). The strategy of associating two signals constitutes a good ability for convenient preliminary screening and accurate diagnosis which assures sensitivity and accuracy (Chuong et al. 2017). Therefore, instead of developing conventional single modality sensors, in the present research, we have worked on engineering the dual-modality biosensor using CdSeTeS-QD@Fe_2O_3 hollow sphere nanoparticles (QD@MHS NPs). Though this kind of novel nanoparticles with magnetic and fluorescence properties have been used in few bio-imaging and drug delivery purpose (Chowdhury et al., 2018; Song et al., 2020), their application for virus detection has not been demonstrated to the best of our knowledge.

Observing the desired need for virus sensing in recent time, a viable embodiment of sensitive and accurate strategies especially for the early stage of infection is in demand which

can give a reliable and accurate signal rapidly. In this work, we describe the application of the synthesized QD@MHS NPs for the development of a dual-modality biosensor for virus detection, incorporating the electrochemical and fluorescence modalities to reduce false signal and self-verification. In real sample analysis, target virus is present together with several interferences clearly displaying the need of magnetic bio-separation. In addition, the rapid sensing signal is obtained from the most commonly used method, fluorescence and these both properties of magnetic and fluorescence are exhibited by QD@MHS NPs. The structures offer a novel platform for target separation from complex biological matrix with significant and reliable signal amplification in clinical diagnosis. Antibody molecules are conjugated onto the surface of QD@MHS NPs to obtain specificity towards the target virus. As shown in **Scheme 1**, target virus could be captured by antibody-functionalized QD@MHS NPs from complex virus samples to form virus/QD@MHS complexes because of the peculiar antigen-antibody reaction (**Scheme 1a**). Virus/QD@MHS complexes and excessive QD@MHS NPs are quickly separated by applying external magnetic field and enriched without any sample pretreatment attributing to the fast-magnetic response of QD@MHS NPs (**Scheme 1b**). After magnetic separation, virus/QD@MHS complexes and free QD@MHS NPs are redispersed in fresh buffer and antibody-labeled reduced graphene oxide modified a gold electrode is introduced into the vial. The virus/QD@MHS complexes are bound to antibodies on the electrode surface and form sandwich structures utilized for electrochemical modality signal readout based on an impedimetric response (**Scheme 1c**). The supernatant is used for fluorescence modality signal readout using the back-calculation method (**Scheme 1d**). The structural merits of the QD@MHS NPs afforded high fluorescence efficiency. Optimizing conditions for sensor formulation and its sensing parameters are investigated thoroughly. This dual-modality sensor relies on specific immunointeractions between target virus and antibody molecules on the surface of QD@MHS NPs. When the antibody-conjugated QD@MHS NPs capture virus and

further binding of this complex on to antibody-conjugated electrode generate the electrochemical signal, but the QDs that unbound by virus utilize to measure the change in fluorescence signal. As the concentration of the virus varies, both the electrochemical impedance and fluorescence signal from the same sensing sample will provide two different signals due to the specific antigen-antibody reactions. The unique structure of QD@MHS NPs offers several advantages for sensitive and accurate detection of biomolecules with significant applications in disease-related diagnostics.

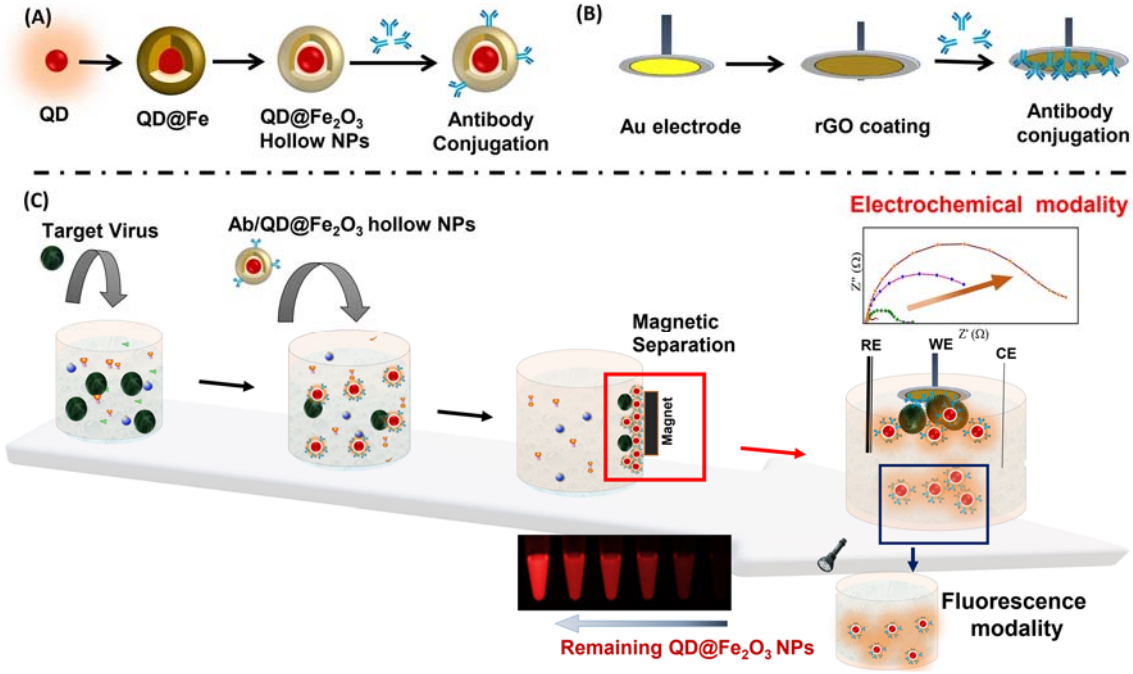

Scheme 1. Schematic representation illustrating the **(A)** fabrication process of QDs encapsulated inside the hollow iron oxide sphere (QD@Fe_2O_3), **(B)** antibody-conjugated rGO-coated Au electrode, and **(C)** target virus detection principle based on antigen-antibody reaction and magnetic separation, using electrochemical impedance and fluorescence as dual-modality. RE, WE, and CE note reference, working, and counter electrodes, respectively.

2. Materials and methods

2.1 Synthesis of CdSeTeS QDs, QD@MHS NP, surface modification of QD@MHS NPs, preparation of antibody-conjugated QD@MHS NPs, characterizations of Synthesized nanoparticles, preparation of HEV-LPs, HEV, NoV-LPs, NoV, Anti-HEV IgG, and Anti-NoV IgG and fabrication of Reduced Graphene Oxide (rGO)-coated gold electrode and antibody binding.

All the above methods are described in detail in the Supplementary data.

2.2 Detection of target viruses.

Antibody-conjugated QD@MHS NPs were mixed with different concentration of the target viruses and further incubated for 10 min. Then an external magnet was placed to separate the target/QD@MHS complex. The external magnet with 1 Tesla used to separate the complex and free QD@MHS from the mixture is a magnetic field gradient. After the separation, the mixture was re-dispersed with into 100 μL PBS fresh buffer using a vortex. Then, Au||rGO/Ab electrodes were incubated with target/QD@MHS complex solution for immunoreaction. After the reaction, the collected supernatant was diluted and the fluorescence intensity was recorded using a fluorescence spectrometer. The incubated electrode was rinsed with ultrapure water and the impedimetric response is measured in the potential EIS mode from 10 kHz to 0.1 Hz with an amplitude of 5 mV.

2.3 Detection of HEV from Fecal Specimens of HEV-infected Cynomolgus Monkey.

A series of fecal specimens were collected from HEV-infected cynomolgus monkey from 4 to 43 dpi (Li et al., 2011). 10% (w/v) suspension of the fecal specimens were prepared by diluting with 10 mM PBS. The mixture was stirred at 4 °C for 1 h, centrifuged at 10,000 × g for

30 min, filtered using a 0.45 µm membrane filter (Millipore, Bedford, MA), and stored at −80 °C for further use. All the samples containing HEV were inactivated before performing sensing by incubating at 70 °C for 20 min. The HEV detection was carried out using the same procedures of the HEV-LPs detection.

3. Results and discussion

3.1 CdSeTeS QDs-encapsulated magnetic hollow sphere nanoparticles synthesis and physicochemical characterizations.

Synthesis of multifunctional nanoparticles using a series of sequential colloidal synthetic procedures with separately optimized steps, resembling the molecular synthesis (Chen et al. 2014; Shevchenko et al. 2008). The synthesis of CdSeTeS QDs encapsulated within magnetic hollow sphere nanoparticles **(**QD@MHS NPs) involves three steps as illustrated in **Fig. 1a**: i) synthesis of CdSeTeS QDs ii), growth of Fe shell on the QDs core, and iii) oxidation of the Fe shell for forming a hollow Fe_2O_3 sphere as explained by Kirkendall effect (Shevchenko et al. 2008; Yin et al., 2004). The preparation commences with the traditional method for synthesis of CdSeTeS QDs core (shown in pink), with excellent fluorescence. The TEM image of CdSeTeS QDs is shown in the **Fig. 1b**. The synthesized CdSeTeS QDs are circular in shape with particle size ranging from 6 to 14 nm and average particle diameter of 10 nm (**Fig. 1c**). Relatively narrow particle size distribution is in corroboration with the optical measurements. Further, metallic iron (shown in brown layer in **Fig. 1a**) is deposited on the surface of the QDs via thermal decomposition of $Fe(CO)_5$. The random deposition of iron onto the surface of the QDs, results in core/shell type structures which is clearly shown in the TEM image (**Fig. 1d)** with an average size of 15 nm (**Fig. 1e**).

200 Passing the O_2/Ar mixture gas through the above prepared core shell QD@Fe solution
201 converts the iron shell into iron oxide via the Kirkendall effect (Yin et al. 2004). Complete
202 oxidation of iron leads to the formation of the void between the QDs core and Fe_2O_3 attributing
203 to the different diffusion rates of oxygen and iron through the outer shell (Shevchenko et al.
204 2008). The complete oxidation of the iron shell on the surface of QDs helps the formation of
205 QD@MHS NPs, which can be clearly seen in TEM image of **Fig. 1f**. After the formation of
206 QD@MHS NPs the average particle size increases to 20 nm (**Fig. 1g**). The empty space
207 between the encapsulated QDs and surrounding hollow Fe_2O_3 is distinctly observable in the
208 high-resolution TEM image (**Fig. 1h)**. HRTEM image of the QD@MHS NP reveals the high
209 crystallinity of the iron oxide shell. The space between Fe_2O_3 hollow sphere and encapsulated
210 QD may restrict charge or energy transfer among both the materials and result in the
211 fluorescence of the QD@MHS NPs, clearly presenting the advantage of hollow structure. The
212 TEM image of synthesized rGO sheet appears as the two-dimensional crumpled thin layers
213 with wrinkled and folded edges (**Fig. S1** of Supplementary data).

214

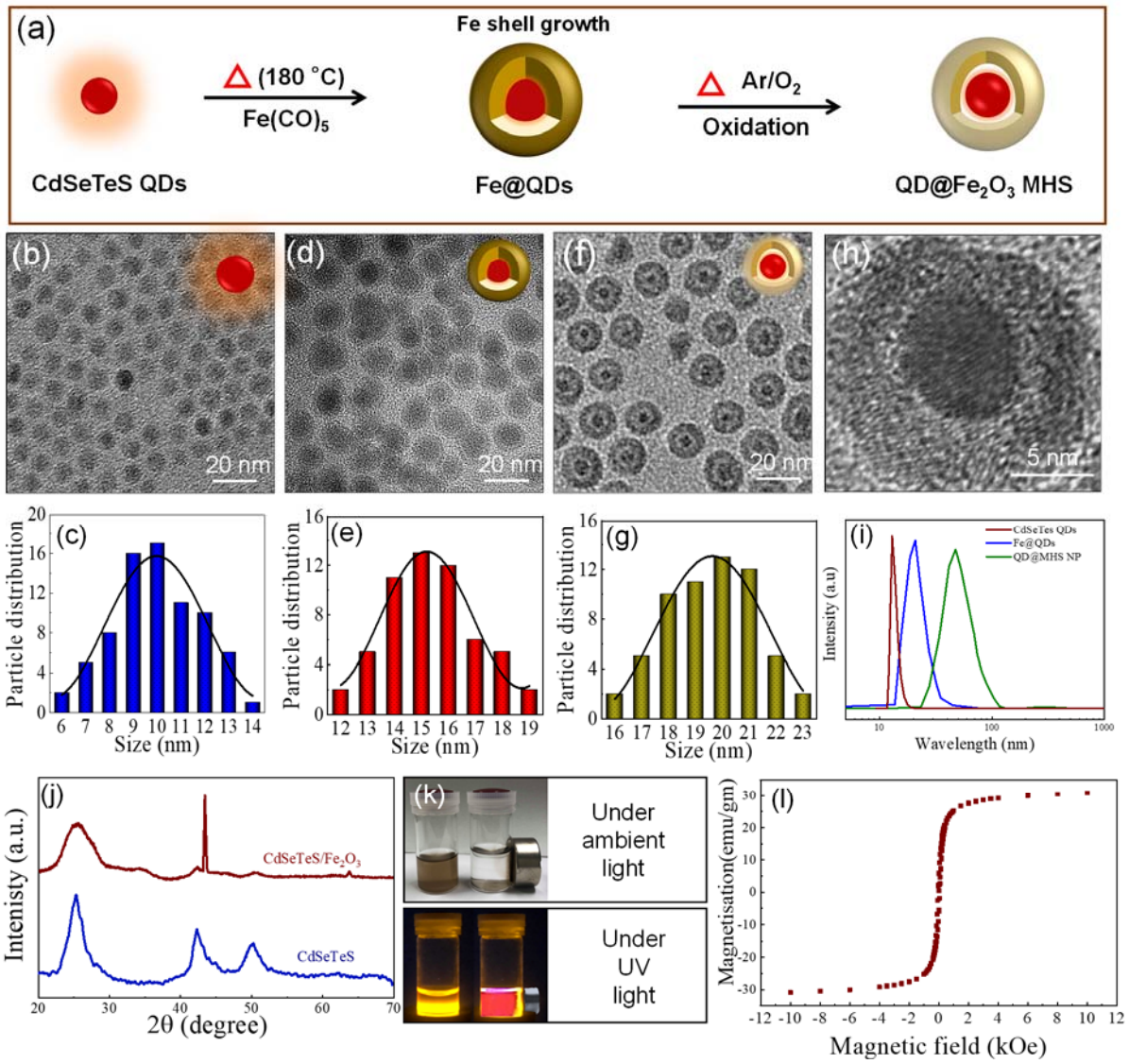

Fig. 1. Synthesis and characterizations of QD@MHS NPs. **(a)** Schematic illustration of the synthesis steps producing the QD@MHS NP. The TEM images of CdSeTeS QDs (**b**), Fe@QDs (metallic iron shell) (**d**) and QD@MHS NP **(f),** and corresponding particle size distributions of CdSeTeS QDs (**c**), Fe@QDs (**e**), and QD@MHS NP (**g**), respectively. High-resolution TEM (HRTEM) image (**h**), DLS measurement of CdSeTeS QDs, Fe@CdSeTeS, and QD@MHS NPs (**i**), XRD pattern (**j**) of QD@MHS NPs. (**k**) Photographs showing the magnetic attraction of CdSeTeS@hollow-Fe_2O_3 in the presence of a magnet under both room and ultraviolet light. (**l**) Saturation magnetization of CdSeTeS@hollow-Fe_2O_3 at 300 K.

The formation of QD@MHS NPs is also confirmed from their hydrodynamic radius found in DLS (**Fig. 1i**). The average size of the synthesized QDs and Fe@QDs is 20 and 25 nm, respectively, indicating the coated Fe shell is around 5 nm. After the oxidation of the iron shell and formation of a hollow structure, the size increases to 50 nm. X-ray diffraction (XRD) is performed to confirm the crystal nature and presence of QDs core and Fe_2O_3. The diffraction pattern of the QDs indicates that the QDs are crystalline and cubic in nature (**Fig. 1j**), exhibiting three characteristic peaks at 2theta of 24.9°, 42.4° and 50.4° for (111), (220), and (311) crystal planes respectively (Adegoke et al., 2015). The position of all these peaks remains unchanged after growth of hollow Fe_2O_3 shell, indicating that the unaffected nature of QDs in the process of iron oxide shell growth. In addition, a clear peak at 2θ of 43.4° appears after the formation of hollow Fe_2O_3 shell on QDs, indicating the successful formation of iron oxide shell on QDs core.

Fig. 1k shows the digital photographs displaying the magnetic and optical properties of QD@MHS NPs. The strong magnetic moment of nanoparticles makes the magnetic separation effective under the external magnetic field. The particles are accumulated on the wall of glass vail immediately after placing external magnet besides the vials containing QD@MHS NPs, leaving the rest of the solution transparent. The fluorescence of synthesized QD@MHS NPs can be clearly observed under the UV lamp.

Magnetic measurements of the as-prepared QD@MHS NPs show a high value of magnetic moment at room temperature (300 K), and the saturation magnetizations of as-prepared nanoparticles is 31.6 emu/g (**Fig. 1l**). The strong magnetic moment of QD@MHS NPs makes the magnetic separation effective under the external magnetic field as shown in **Fig. 1k**. This is in good agreement with other gold/iron oxide core/hollow-shell nanocomposites with various morphological characterizations (Shevchenko et al. 2008).

249 The formation of QD@MHS NPs is further characterized by XPS analysis. The survey
250 scan of as-prepared QD@MHS NPs clearly shows the characteristic peaks of Se 3d (52.9 eV),
251 S 2p (163.3 eV), C 1s (284.7 eV), Cd 3d (405.7 eV), O 1s (532.1 eV), Te 3d (582.9 eV) and
252 Fe 2p (711.5 and 725.1 eV) (**Fig. 2a**). **Fig. 2b** shows the Cd 3d spectra of QDs and QD@MHS
253 NPs. Superposition of these two spectra shows that the phase of the Cd 3d is not much affected
254 even after the formation of hollow iron oxide sphere on the surface of QDs. The peak
255 deconvolution of Fe 2p spectra of QD@MHS NPs is further performed (**Fig. 2c**). The
256 characteristic peaks of Fe $2p_{3/2}$ and Fe $2p_{1/2}$ centered at 710.9 and 724.8 eV, respectively,
257 confirm the formation of Fe_2O_3 in the composites (Lv et al., 2015). The deconvolution of the
258 spectra shows two main peaks at 710.3 and 712.5 eV, which belong to Fe^{3+} and Fe^{2+},
259 respectively. Additionally, weak satellite bands associated with these main peaks are detected,
260 with the one from Fe $2p_{3/2}$ being at 718.5 eV which is characteristic of Fe^{3+} species. The
261 deconvoluted Fe XPS spectra domains leave the possibility of the coexistence of Fe_2O_3 and
262 Fe_3O_4 (Lv et al. 2015).

263 The UV/Vis spectrum of the synthesized QD@MHS NPs in **Fig. 2d** shows the signature
264 absorption hump of CdSeTeS QDs even after the growth of hollow iron shell which confirms
265 the successful synthesis. The fluorescent spectra of QD@MHS NPs and pure QDs are
266 compared as shown in **Fig. 2e**. In spite of a little broadened of the peak, the FL spectra of the
267 QD@MHS NPs shows identical peak maxima to that of the unmodified QDs, indicating that
268 the average core size is preserved despite the oxidation procedure. The quantum yield of the
269 fluorophore is a crucial parameter to develop a sensitive fluorometric sensing system
270 (Ganganboina et al. 2018). The quantum yield of QD@MHS NPs, measured by using
271 fluorescein as the standard, is optically determined to be 17%, which is satisfactory to serve as
272 the fluorometric sensing probe for virus detection.

273

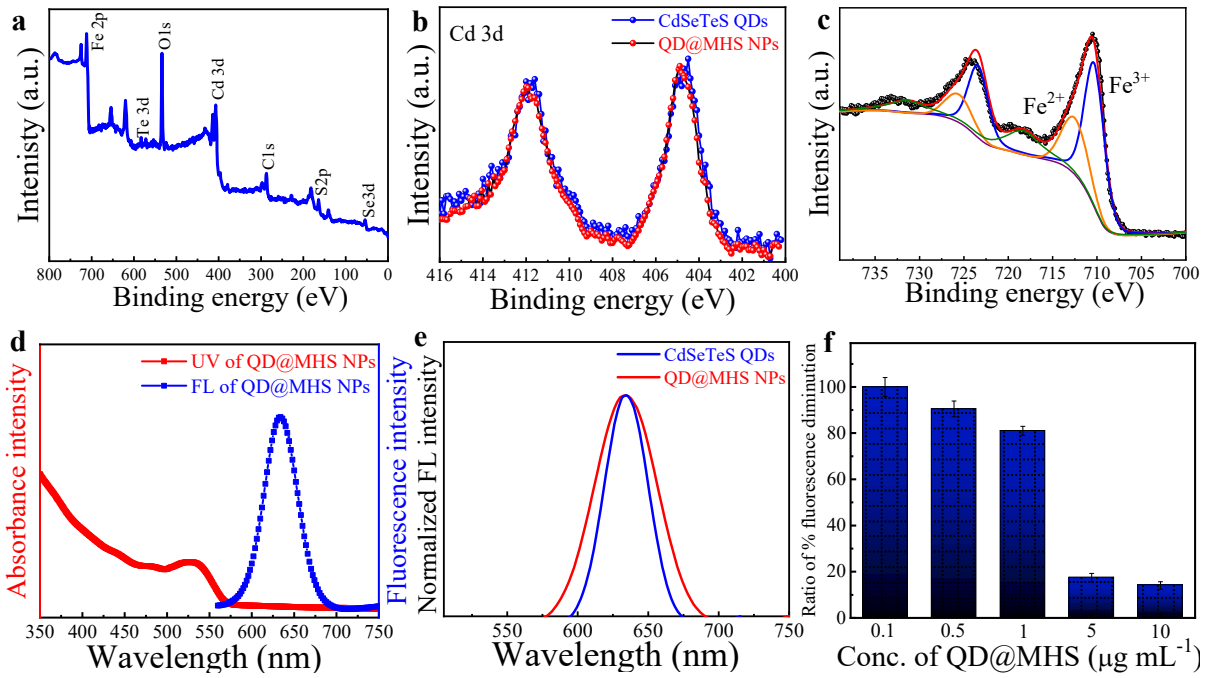

Fig. 2. (**a**) XPS survey spectra of synthesized QD@MHS NPs, **(b)** Cd 3d spectra of bare QDs and QD@MHS NPs, **(c)** deconvoluted XPS spectra of Fe 2p, **(d)** absorption and fluorescence spectra of synthesized QD@MHS NPs, **(e)** fluorescence of bare CdSeTeS and QD@MHS NPs and **(f)** effect of QD@MHS NPs concentration on fluorescence intensity in presence of 1 ng mL^{-1} of HEV-LPs.

3.2 Working principle for virus detection using dual-modality readout.

Scheme 1 shows the essential principal of the newly developed dual-modality sensing method for robust and ultrasensitive detection of target virus. It comprises of specific antibody-conjugated QD@MHS NPs which can specifically recognize the target virus and can form complexes. Thus, formed complex and free QD@MHS are separated from the mixture by magnetic separation and dispersed into fresh buffer. Further, Au||rGO/antibody electrode is introduced and incubated with above separated solution. The antibody on the electrode surface is capable of specifically capturing the complex of target virus and QD@MHS NPs and the

electrode is removed from the above solution and used for measuring the impedimetric response. After target virus and QD@MHS NPs conjugation on the electrode surface, several non-conducting viruses reduced the conductivity of Au||rGO/antibody electrode, resulting in an increase in the charge transfer resistance. The change in the charge transfer resistance of the Au||rGO/antibody electrode incubated with various target virus concentrations can be used for detection of virus.

The QD@MHS NPs have excellent fluorescence performance due to the presence of QDs inside the hollow iron oxide shell. We further used the fluorescence modality which can ensure sensitivity and accuracy of target virus. The supernatant containing free QD@MHS NPs is used to record the fluorescence intensity. The increase in the concentration of target virus facilitates the binding of increased number of QD@MHS NPs with target virus and further with Au||rGO/antibody electrode, resulting in the decrease of fluorescence intensity. The absence of target virus cannot form the target/QD@MHS complex resulting in insufficient hindrance for the electrode to generate resistance and further decrease the fluorescence intensity of supernatant. In sum, the developed sensor based on QD@MHS NPs constructed a dual-modality assay composed of a fluorescence and an electrochemical impedimetric signal.

The effect of QD@MHS NPs concentration on change in fluorescence intensity after target addition is investigated. For the optimization of sensing parameters, five concentrations of anti-HEV antibody-conjugated QD@MHS NPs (0.1, 0.5, 1, 5 and 10 μg mL^{-1}) are used. The formation of target virus/QD@MHS NPs complexes is tested with HEV-LPs of 1 ng mL^{-1}. It is evident from **Fig. 2f** that the ratio of fluorescence diminution is very low for 5 and 10 μg mL^{-1} of QD@MHS NPs as excess amount of QD@MHS NPs are present in comparison to HEV-LPs, other three concentrations show significant change in the ratio of fluorescence diminution. The fluorescence of the lowest concentration, 0.1 μg mL^{-1} has completely diminished, as almost all QD@MHS NPs were bound to HEV-LPs and further bound to rGO

coated Au electrode. Therefore, the high concentrations of 10 and 5 μg mL^{-1} and low concentration of 0.1 μg mL^{-1} are not suitable for this sensing strategy. In addition, the overall ratio of % fluorescence diminution at 1 μg mL^{-1} QD@MHS NPs is quite comparable with that at the 0.5 μg mL^{-1}. The ratio of % fluorescence decreases in the 1 μg mL^{-1} QD@MHS NPs is high in comparison with that in the 0.5 μg mL^{-1} allowing the increased linear range of detection. We have also optimized the QD@MHS NPs concentration using various concentrations of HEV-LPs (**Fig. S2** of Supplementary data). After all the optimization experiments, we have chosen the QD@MHS NPs concentration of 1 μg mL^{-1} as the optimum for further studies.

The electrochemical performance of the stepwise immobilization procedure of the proposed sensor is performed in the $K_3Fe(CN)_6^{3-/4-}$ system in a potential window range from − 0.2 to 0.6 V at a scan rate of 100 mV s^{-1}. The peak intensity of $Fe(CN)_6^{3-/4-}$ at + 0.16/+ 0.27 V of the Au||rGO electrode decreases gradually when biomolecules including anti-HEV and HEV-LPs are added onto rGO modified Au electrode **(Fig. S3** of Supplementary data**)**, which attributed to the fact that the attachment of biomolecules inhibits the electron transfer process. The decreasing tendency in peak intensity obtained from the CV curve is conclusive to the electroactivity of the developed sensing probe. This phenomenon is mainly attributed to the fact that the charge transfer between electrolyte and the surface of Au||rGO electrode is hindered partially by the immobilization of anti-HEV and HEV-LPs.

3.3 Sensitive detection of target virus with dual-modality readout.

For proof of concept, the HEV-LPs are detected by the dual-modality readout after integrating with the high-efficiency immune magnetic separation. Fluorescence and electrochemical signal changes caused by concentration changes of HEV-LPs are recorded to discuss the linear analytic range. Initially, different concentrations of HEV-LPs are mixed with

anti-HEV antibody-conjugated QD@MHS NPs. The change in electrochemical impedance spectroscopy (EIS) response of Au||rGO/anti-HEV electrodes at various concentrations of HEV-LPs is shown in **Fig. 3a**. The detection of HEV-LPs using electrochemical modality is based on the degree of increased impedance of electrode, which is attributed to the formation of Au||rGO/anti-HEV/HEV-LPs bio-conjugate on the electrode surface. The diameter of semicircle in Nyquist plot, which represents the charge transfer resistance at the electrode electrolyte interface (R_{ct}), becomes large after the addition of HEV-LPs, indicating the increase in resistance caused by the binding of large number of virus onto the electrode surface (Chowdhury et al., 2019). Moreover, the R_{ct} increases gradually with the increase in HEV-LPs concentrations from 10 fg mL^{-1} to 10 ng mL^{-1}. The equivalent circuit diagram used to fit the frequency range of 10 kHz–0.1 Hz is depicted in **Fig. S3** of Supplementary data. The fitted values of parameters at various HEV-LPs concentrations are shown in **Table S1** of Supplementary data. A significant change in R_{ct} is clearly observed after the addition of 10 fg mL^{-1} to 10 ng mL^{-1} HEV-LPs. **Fig. 3b** shows the calibration curve of HEV-LPs and a good linear relationship between change in R_{ct} and HEV-LPs concentration in the range of 10 fg mL^{-1} to 10 ng mL^{-1} is observed. The limit of detection (LOD), determined by the 3σ/S (Ganganboina and Doong 2019) where σ is the standard deviation of the lowest signal and S is the slope of linear calibration plot, is 1.2 fg mL^{-1}.

Utilizing the fluorescence property of QD@MHS NPs, we could also use the fluorescence modality for ultrasensitive detection and accurate diagnosis. Thus, after all the HEV-LPs/QD@MHS complexes are conjugated to the electrode, while the supernatant consisting of remaining QD@MHS NPs is used to measure the fluorescence intensity. **Fig. 3c** shows the decrease in fluorescence spectra at 630 nm as the concentration of HEV-LPs increases from 10 fg mL^{-1} to 10 ng mL^{-1}. Good linear relationship between change in fluorescence intensity and logarithmic values of HEV-LPs concentration with a correlation coefficient (R^2) of 0.992 is

obtained in the linear range of HEV-LPs from 10 fg mL^{-1} to 10 ng mL^{-1} (**Fig. 3d**). The LOD is calculated to be 2.6 fg mL^{-1} as determined by the 3σ/S (Ganganboina and Doong 2019).

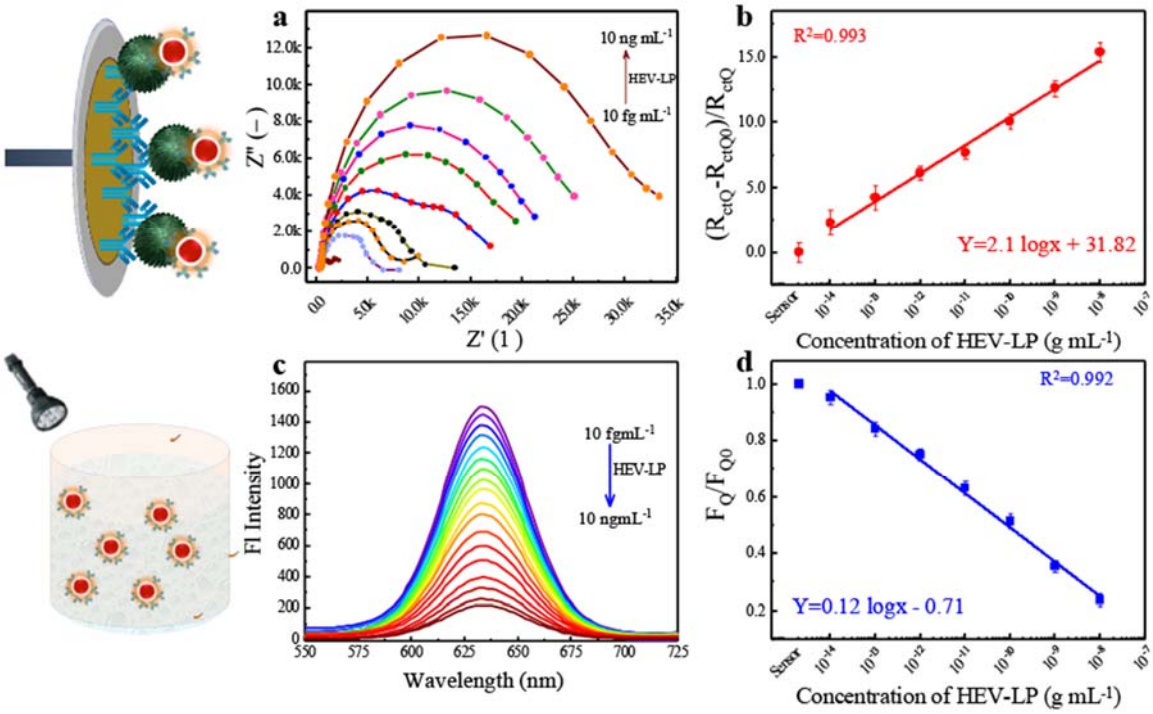

Fig. 3. Sensitivity test of QD@MHS NPs based dual-modality sensor for HEV-LPs sensing. **(a)** Nyquist plot of Au||rGO/anti-HEV antibody at various concentrations of HEV-LPs ranging from 10 fg mL^{-1} to 10 ng mL^{-1}, (**b**) calibration curve for detection of HEV-LPs, change in charge transfer resistance and concentration of HEV-LPs, **(c)** fluorescence spectra of QD@MHS NPs in the presence of different concentrations of HEV-LPs and (**d**) calibration curve, change of fluorescence intensities of QD@MHS NPs vs. concentration of HEV-LPs. The sensor in the x-axis of **b** and **d** denotes the responses of electrode and supernatant containing free QD@MNS NPs without analytes, respectively.

The developed detection strategy is universal and can be straightforwardly extended to the specific detection of other types of viruses. In order to further prove the sensitivity and accuracy of the developed dual-modality sensor, we have performed the detection of NoV-LPs using both impedimetric and fluorescence modality. **Fig. 4a** shows the Nyquist plots of the sensor electrode with respect to the increasing concentrations of NoV-LP in the range of 10 fg mL^{-1} to 10 ng mL^{-1}. It can be clearly observed that the diameter of semicircle, which represents the R_{ct}, increases upon the NoV-LPs/QD@MHS complex, which indicates the increase in resistance caused by the NoV-LPs onto the electrode surface. The supernatant was collected for fluorescence measurements, and the fluorescence intensity at 630 nm decreased as the NoV-LPs concentration increased (**Fig. 4b**). The excellent linear correlation appeared from 10 fg mL^{-1} to 10 ng mL^{-1} with an R^2 of 0.991 and 0.989 on electrochemical impedance and fluorescence modality, respectively (**Fig. 4c**). The sensitivity of the developed dual-modality sensor for virus detection is competitive with recently developed analytical sensing methods comprising electrochemical and optical methods (**Table S2** of Supplementary data) (Chowdhury et al. 2019; Hwang et al., 2017; Jothikumar et al., 2006; Khoris et al., 2019; Takemura et al., 2017; Wang et al., 2010; Zeng et al., 2012). These results indicate that the developed dual-modality sensor for detections of virus exhibits benefits including ultra-sensitivity of electrochemical method and wide linear range detection, which can offer accurate and reliable quantitative results.

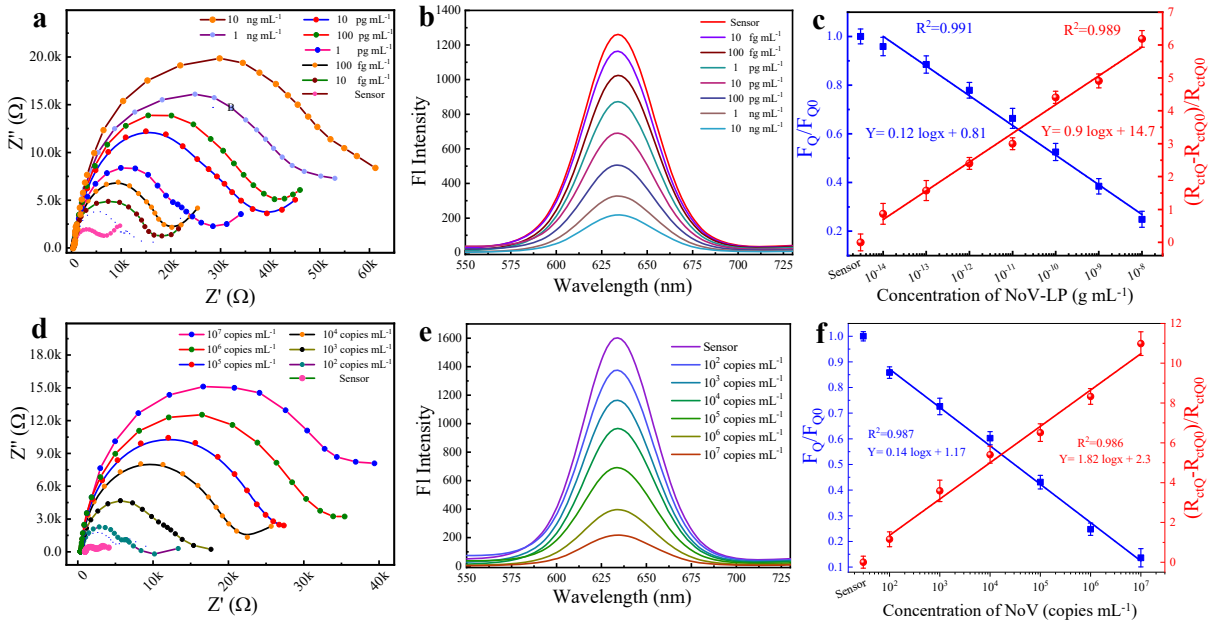

Fig. 4. Detection of NoV-LPs (**a–c**) and NoV from clinical specimens (**d–f**). (**a, d**) EIS spectra of different concentrations, **(b, e**) fluorescence curves, and (**c, f**) dual-modality calibration curve, change of fluorescence intensity of QD@MHS NPs and charge transfer resistance of Au||rGO/antibody electrode vs concentration of NoV-LPs (**a–c**) and NoV from clinical specimens (**d–f**). The sensor in x-axis of **c** and **f** denotes the responses of electrode and supernatant containing free QD@MNS NPs without analytes, respectively.

3.4 Dual-modality readout for norovirus from clinical specimens.

Encouraged by the high sensitivity and accuracy of the QD@MHS NPs based dual-modality assay, to confirm the practicability real clinical samples are examined. As shown in **Fig. 4d**, the impedimetric response increases with the increase in NoVs GII. 3 concentrations obtained from human feces. The impedance continuously increases with the increase in concentration of NoV GII. 3 from 10^2 to 10^7 RNA copies mL^{-1}. In addition, the fluorescence intensity at 630 nm continuously decreases in the collected supernatant (**Fig. 4e**). The excellent linear correlation appeared from 10^2 to 10^7 RNA copies mL^{-1} with R^2 of 0.987 and 0.986 on

electrochemical impedance and fluorescence modality, respectively (**Fig. 4f**). The LOD of NoV is measured to be 69 RNA copies mL^{-1}.

3.5 Detection of HEVs from cell culture supernatant and from fecal specimens of HEV-infected monkey.

To evaluate the performance of the developed dual-modality sensor for detection of HEV from cell culture supernatant, the impedimetric and fluorometric responses are recorded. The charge transfer value continuously increased with the increase in concentration of HEV from 10^2–10^7 RNA copies mL^{-1} and the decrease in intensity of fluorescence signal is observed. As shown in **Fig. 5a,** HEV shows a correlation coefficient (R^2) of 0.988 in electrochemical modality and 0.987 in fluorescence modality. The LOD for HEV is measured to be 57 RNA copies mL^{-1}. These results strongly demonstrate that our dual-modality sensor possesses a strong anti-interference ability, high accuracy as well as high sensitivity.

Considering the high sensitivity and accuracy of developed dual-modality assay, it is further applied to evaluate the applicability in fecal specimens of HEV-infected cynomolgus monkey (Li et al., 2016b). Fecal specimens are collected from 4–43 days-post-infection (dpi). The infection peak is shown within the first to second week and then gradually decreased to undetectable amount as observed from the RNA copy numbers measured by RT-qPCR. Further, the times series change in impedance and fluorescence signal using the developed dual-modality sensor is recorded. The RT-qPCR data in **Fig. 5b** show that the HEV RNA is detectable in fecal specimens until 22 dpi. Based on the infection cycle of HEV and the result of the RT-qPCR, the HEV RNA is undetectable in the samples collected after 22 dpi. Therefore, the fecal samples collected after 22 dpi are considered as the negative control. The trend of the obtained result from the QD@MHS NPs-based dual-modality sensor is similar with the RT-

qPCR results, confirming the applicability of developed dual-modality sensing method for real samples. This dual-modality strategy builds a useful capability for both fluorescence-based convenient preliminary screening and electrochemical-based accurate diagnosis of suspect infections.

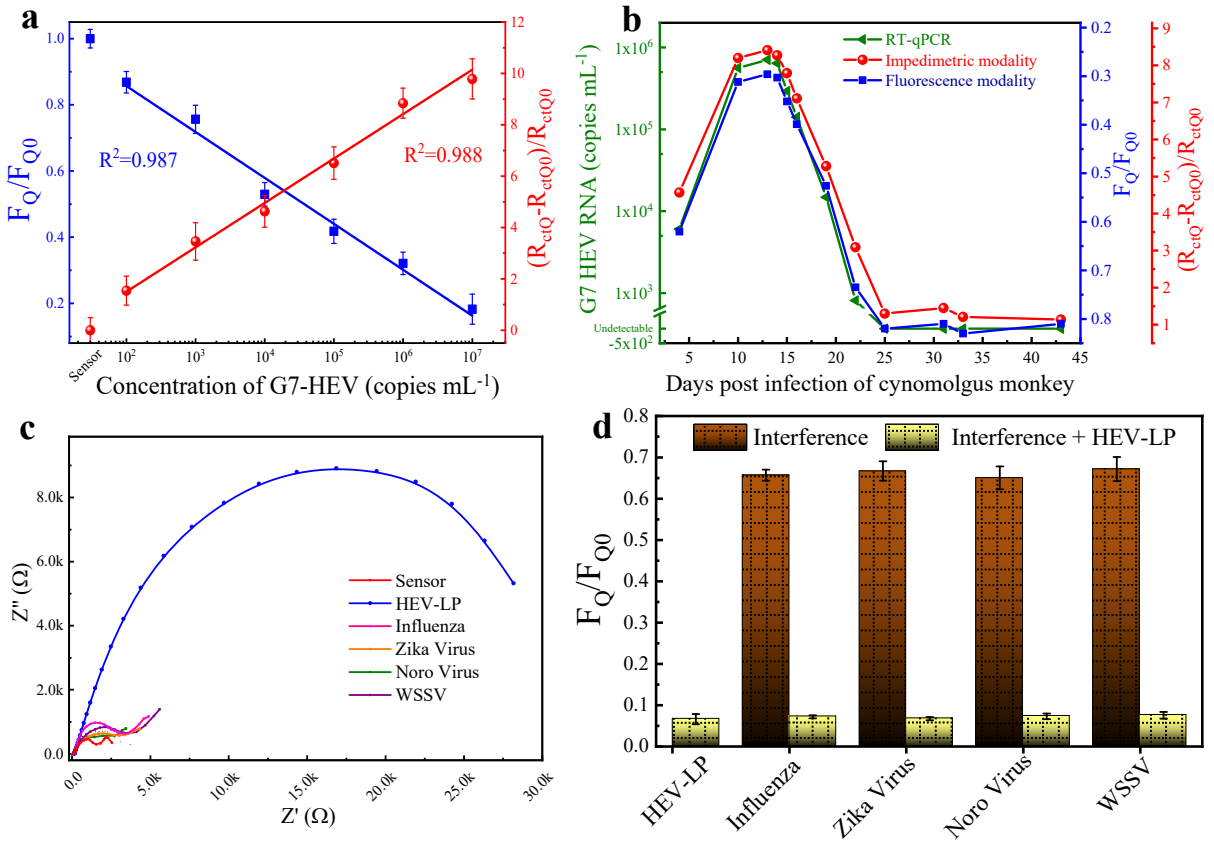

Fig. 5. (**a**) Detection of G3 HEV in cell culture supernatants using dual-modality sensor, (**b**) Comparison of the sensitivity among the dual-modality sensor and RT-qPCR by detection of HEV in fecal samples of cynomolgus macaque monkey collected from collected at 4–43 pdi, (**c**) change in charge transfer resistance and (**d**) fluorescence intensity of Au||rGO/anti-HEV electrode and QD@MHS NPs in the presence of the target HEV-LPs and other common interferences. The sensor in x-axis of **a,** denotes the responses of electrode and supernatant containing free QD@MNS NPs without analytes, respectively. WSSV: white spot syndrome virus.

To evaluate the applicability of the developed dual-modality sensor in a sophisticated biological sample matrix, human serum is used as a detection medium. HEV-LPs spiked samples with various concentrations show a similar trend of detection, confirming the application of the developed sensor for the clinical sample monitoring (**Fig. S5** of supplementary data). Interestingly, the sensitivity achieved in the complex medium like serum showed only a slight difference, with similar linearity of their calibration plots. This can be attributed to the magnetic separation used in the detection procedure, which enriches the analyte separating from other interfering molecules.

3.6 Specificity of dual-modality sensor.

The interaction between the target virus with the QD@MHS NPs and Au||rGO/antibody is governed by the antibody conjugation. Anti-HEV antibody is conjugated to QD@MHS NPs and Au||rGO electrode for the proof of concept. To confirm the specificity of the proposed sensor the selectivity experiment is carried out in presence of serum medium using 10% diluted human serum using influenza virus, NoV, white spot syndrome virus (WSSV) and zika virus as other samples. **Fig. 5c** shows the impedimetric response of Au||rGO/anti-HEV antibody electrode to the mixture of negative samples. The sensors in buffer and 100% serum (as negative control) do not show any significant change in signal attributing to the magnetic separation of virus complex effectively separating the interferences. The increase in impedance value is observed only in the HEV-LPs sample and no obvious change is observed in the other samples. Only small increase in impedance from 0.5 – 5% in all the negative samples clearly indicating the superior specificity of developed dual-modality sensor.

In addition, the selectivity of the developed sensor for HEV-LPs is also measured by fluorescence modality. **Fig. 5d** shows the fluorescence of developed immunosensor to the

mixture of negative samples and HEV-LP. Fluorescence intensity decreases only in the presence of target HEV-LP (**Fig. 5d**) as QD@MHS NPs are unable to conjugate interfering samples further cannot conjugate to Au||rGO/Anti-HEV antibody electrode. As a result, after separation, there is no change in the amount of nanoparticles resulting negligible change in the fluorescence. These results show that the developed dual-modality sensor is highly specific for HEV-LP detection.

In comparison with regular single modality assay, dual-modality sensor using QD@MHS NPs exhibits the below benefits. In this dual-modality sensor electrochemical impedance and fluorescence sensing modalities are merged into single sensing system, benefiting the wide linear range sensing with significantly enhanced sensitivity and increased accuracy. QD@MHS NPs serve as bifunctional probes comprised of an optically active semiconductor QD core with high fluorescence, encapsulated within a hollow iron oxide sphere allowing the bioseparation. The unique morphology of QD@MHS NPs prevents unwanted interactions within the nanoparticles which may abrogate the fluorescence and magnetic properties. The magnetic property helps in separating the virus from the strong sample matrix allows negligible background noise and may help in exhibiting strong anti-interference ability and accuracy. Further, from a sample consumption perspective, the required sample volume used in the presented integrated dual-modality sensor is less than that used in two spatially separated electrochemical and fluorescence sensors. Finally, the developed dual-modality sensor avoids the complicated sample preparation and limits the use of sophisticated analytical equipment presenting a unique platform for significant applications in disease diagnostics. The present integrated dual-modality sensor incorporates both electrochemical and fluorescence detection methods on a single nanocomplex for recognizing and quantifying virus. The integrated dual-modality design potentially will help increase detection reliability due to the ability of the

sensor to generate two readouts for a specific antigen-antibody reaction at the QD@MHS NPs surface.

4. Conclusions

In summary, we have demonstrated an approach and effective method for assembling QD@MHS NPs, profiting by integrating of dual-modality sensing with electrochemical and fluorescence readout in a single detection system. The unique morphology of QD@MHS NPs preserves the fluorescence of the incorporated QDs and also provides the magnetic property from the hollow sphere. Strong magnetic responsive ability of QD@MHS NPs, favours the efficient target separation from complex samples without any pre-treatment. The NPs has successfully applied for the low-level virus detection, applying the universal antigen antibody conjugation. As a result, amplified electrochemical modality signal from the virus loaded QD@MHS NPs working electrode and fluorescence readout from supernatant with only the remaining QD@MHS NPs is attained. The HEV-LPs can be specifically assayed by dual-modality sensor with a detection limit down to 1.2 fg mL^{-1}. Importantly, this developed sensor showed excellent performance for real clinical sample diagnosis in complex matrix without eliciting observable interference. In addition, it is successfully applied for the detection of fecal samples from HEV-infected monkey and found sensitivity similar to that data obtained from RT-qPCR. We envision that other viruses can also be detected by simple changing the conjugated antibodies with the QD@MHS NPs which may spur major progress in dual-modality sensor for precise virus diagnosis.

CRediT authorship contribution statement

Akhilesh Babu Ganganboina: Conceptualization of this study, Methodology, Investigation, Writing the manuscript. **Ankan Dutta Chowdhury:** Data analysis, Revision of manuscript. **Indra Memdi Khoris:** Investigation. **Ruey-an Doong:** Resources. **Tian-Cheng Li**: Resources. **Toshimi Hara:** Resources. **Fuyuki Abe:** Resources. **Tetsuro Suzuki:** Resources. **Enoch Y. Park:** Conceptualization, Supervision, Revision of manuscript.

Declaration of competing interest

The authors declare that they have no competing financial interests.

Acknowledgement

We thanks to Professor K. Morita of Institute of Tropical Medicine Nagasaki University and Dr. Jun Satoh of National Research Institute of Aquaculture of Japan Fisheries Research and Education Agency for providing Zika virus (strain PRVABC-59) and white spot syndrome virus (WSSV), respectively, for the selectivity test. A.B.G. and A.D.C sincerely thanks the Japan Society for the Promotion of Science (JSPS) for a postdoctoral fellowship (Grant Nos. 19F19064 and 17F17359).

Appendix A. Supplementary data

Supplementary data associated with this article can be found in the online version at:

References

Adegoke, O., Nyokong, T., Forbes, P.B., 2015. J. Alloys Compd. 645, 443–449.

Alivisatos, P., 2004. Nat. Biotechnol. 22(1), 47–52.

Boldt, K., Jander, S., Hoppe, K., Weller, H., 2011. ACS Nano 5(10), 8115–8123.

Bruns, O.T., Ittrich, H., Peldschus, K., Kaul, M.G., Tromsdorf, U.I., Lauterwasser, J., Nikolic, M.S., Mollwitz, B., Merkel, M., Bigall, N.C., 2009. Nat. Nanotechnol. 4(3), 193–201.

Chen, O., Riedemann, L., Etoc, F., Herrmann, H., Coppey, M., Barch, M., Farrar, C.T., Zhao, J., Bruns, O.T., Wei, H., 2014. Nature commun. 5, 5093.

Chen, Z., Mu, X., Han, Z., Yang, S., Zhang, C., Guo, Z., Bai, Y., He, W., 2019. J. Am. Chem. Soc. 141(45), 17973–17977.

Cho, M., Contreras, E.Q., Lee, S.S., Jones, C.J., Jang, W., Colvin, V.L., 2014. J. Phys. Chem. C 118(26), 14606–14616.

Chowdhury, A.D., Ganganboina, A.B., Tsai, Y.C., Chiu, H.-c., Doong, R.A., 2018. Anal. Chim. Acta 1027, 109–120.

Chowdhury, A.D., Takemura, K., Li, T.-C., Suzuki, T., Park, E.Y., 2019. Nature Commun. 10, 3737.

Chuong, T.T., Pallaoro, A., Chaves, C.A., Li, Z., Lee, J., Eisenstein, M., Stucky, G.D., Moskovits, M., Soh, H.T., 2017. Proc. Natl. Acad. Sci. U.S.A. 114(34), 9056–9061.

Dang, D.V., Ganganboina, A.B., Doong, R.A., 2020. ACS Appl. Mater. Interfaces 12(29), 32247–32258.

Feld, A., Merkl, J.P., Kloust, H., Flessau, S., Schmidtke, C., Wolter, C., Ostermann, J., Kampferbeck, M., Eggers, R., Mews, A., 2015. Angew. Chem. Int. Ed. 54(42), 12468–12471.

Ganganboina, A.B., Doong, R.A., 2018. Microchim. Acta 185(11), 526.

Ganganboina, A.B., Doong, R.A., 2019. Sci. Rep. 9(1), 7214.

566 Ganganboina, A.B., Dutta Chowdhury, A., Doong, R.A., 2018. ACS Appl. Mater. Interfaces
567 10(1), 614–624.
568 Ganganboina, A.B., Dutta Chowdhury, A., Khoris, I. M., Nasrin, F., Takemura, K., Hara, T.,
569 Abe, F., Suzuki, T., Park, E. Y., 2020. Biosens. Bioelectron. 157, 112169.
570 Hwang, H.J., Ryu, M.Y., Park, C.Y., Ahn, J., Park, H.G., Choi, C., Ha, S.D., Park, T.J., Park,
571 J.P., 2017. Biosens. Bioelectron. 87, 164–170.
572 Jothikumar, N., Cromeans, T.L., Robertson, B.H., Meng, X., Hill, V.R., 2006. J. Virol.
573 Methods 131(1), 65–71.
574 Juárez, B.H., Klinke, C., Kornowski, A., Weller, H., 2007. Nano Lett. 7(12), 3564–3568.
575 Khoris, I.M., Takemura, K., Lee, J., Hara, T., Abe, F., Suzuki, T., Park, E.Y., 2019. Biosens.
576 Bioelectron. 126, 425–432.
577 Kim, J., Lee, J.E., Lee, J., Yu, J.H., Kim, B.C., An, K., Hwang, Y., Shin, C.-H., Park, J.-G.,
578 Kim, J., 2006. J. Am. Chem. Soc. 128(3), 688–689.
579 Lee, N., Yoo, D., Ling, D., Cho, M.H., Hyeon, T., Cheon, J., 2015. Chem. Rev. 115(19),
580 10637–10689.
581 Li, C.M., Zhan, L., Zheng, L.L., Li, Y.F., Huang, C.Z., 2016a. Analyst 141(10), 3020–3026.
582 Li, T.-C., Yoshimatsu, K., Yasuda, S.P., Arikawa, J., Koma, T., Kataoka, M., Ami, Y., Suzaki,
583 Y., Mai, L.T.Q., Hoa, N.T., 2011. J. Gen. Virol. 92(Pt 12), 2830.
584 Li, T.-C., Zhou, X., Yoshizaki, S., Ami, Y., Suzaki, Y., Nakamura, T., Takeda, N., Wakita, T.,
585 2016b. J. Hepatol. 65(6), 1104–1111.
586 Lv, H., Zhao, H., Cao, T., Qian, L., Wang, Y., Zhao, G., 2015. J. Mol. Catal. A: Chem. 400,
587 81–89.
588 Milliron, D.J., Hughes, S.M., Cui, Y., Manna, L., Li, J., Wang, L.-W., Alivisatos, A.P., 2004.
589 Nature 430(6996), 190–195.

590 Oh, S., Kim, J., Tran, V.T., Lee, D.K., Ahmed, S.R., Hong, J.C., Lee, J., Park, E.Y., Lee, J.,
591 2018. ACS Appl. Mater. Interfaces 10(15), 12534–12543.
592 Park, J., Jeong, Y., Kim, J., Gu, J., Wang, J., Park, I., 2020. Biosens. Bioelectron. 148, 111822.
593 Shevchenko, E.V., Bodnarchuk, M.I., Kovalenko, M.V., Talapin, D.V., Smith, R.K., Aloni, S.,
594 Heiss, W., Alivisatos, A.P., 2008. Adv. Mater. 20(22), 4323–4329.
595 Shrivastava, S., Trung, T.Q., Lee, N.-E., 2020. Chem. Soc. Rev. 49, 1812–1866.
596 Song, L., Wang, Z., Liu, J., Wang, T., Jiang, Q., Ding, B., 2020. ACS Appl. Bio Mater. 3(5),
597 2854–2860.
598 Takemura, K., Adegoke, O., Takahashi, N., Kato, T., Li, T.-C., Kitamoto, N., Tanaka, T.,
599 Suzuki, T., Park, E.Y., 2017. Biosens. Bioelectron. 89, 998–1005.
600 Wang, X., Li, Y., Wang, H., Fu, Q., Peng, J., Wang, Y., Du, J., Zhou, Y., Zhan, L., 2010.
601 Biosens. Bioelectron. 26(2), 404–410.
602 Wu, Z., Zeng, T., Guo, W.-J., Bai, Y.-Y., Pang, D.-W., Zhang, Z.-L., 2019. ACS Appl. Mater.
603 Interfaces 11(6), 5762–5770.
604 Xiong, L.-H., He, X., Zhao, Z., Kwok, R.T., Xiong, Y., Gao, P.F., Yang, F., Huang, Y., Sung,
605 H.H.-Y., Williams, I.D., 2018. ACS Nano 12(9), 9549–9557.
606 Yin, Y., Rioux, R.M., Erdonmez, C.K., Hughes, S., Somorjai, G.A., Alivisatos, A.P., 2004.
607 Science 304(5671), 711–714.
608 Zeng, Q., Zhang, Y., Liu, X., Tu, L., Kong, X., Zhang, H., 2012. Chem. Comm. 48(12), 1781–
609 1783.

610

Supplementary data

Hollow magnetic-fluorescent nanoparticles for dual-modality virus detection

Akhilesh Babu Ganganboina,[1] Ankan Dutta Chowdhury,[1] Indra Memdi Khoris,[2] Ruey-an Doong,[3] Tian-Cheng Li,[4] Toshimi Hara,[5] Fuyuki Abe,[5] Tetsuro Suzuki,[6] Enoch Y. Park[1,2,*]

[1] Research Institute of Green Science and Technology, Shizuoka University, 836 Ohya Suruga-ku, Shizuoka 422-8529, Japan

[2] Department of Bioscience, Graduate School of Science and Technology, Shizuoka University, 836 Ohya Suruga-ku, Shizuoka 422-8529, Japan

[3] Institute of Analytical and Environmental Sciences, 101, Section 2, Kuang-Fu Road, National Tsing Hua University, Hsinchu 30013, Taiwan

[4] Department of Virology 2, National Institute of Infectious Diseases, 4-7-1 Gakuen, Musashimurayam-shi, Tokyo 208-0011, Japan

[5] Department of Microbiology, Shizuoka Institute of Environment and Hygiene, 4-27-2, Kita-ando, Aoi-ku, Shizuoka 420-8637, Japan

[6] Department of Infectious Diseases, Hamamatsu University School of Medicine, 1-20-1 Higashi-ku, Handa-yama, Hamamatsu 431-3192, Japan

E-mail addresses:
akhilesh.babu.ganganboina@shizuoka.ac.jp (ABG)
ankan.dutta.chowdhury@shizuoka.ac.jp (ADC)
Indra.memdi.khoris.17@shizuoka.ac.jp (IMK)
radoong@mx.nthu.edu.tw (RAD)
litc@nih.go.jp (TCL)
toshimi1_hara@pref.shizuoka.lg.jp (TH)
fuyuki1_abe@pref.shizuoka.lg.jp (FA)
tesuzuki@hama-med.ac.jp (TS)
park.enoch@shizuoka.ac.jp (EYP)

[*] Corresponding author at: Research Institute of Green Science and Technology, Shizuoka University, 836 Ohya, Suruga-ku, Shizuoka 422-8529, Japan.
E-mail address: park.enoch@shizuoka.ac.jp (E.Y. Park). Tel (Fax): +81-54-238-4887)

1 Experimental methods

1.1 Synthesis of CdSeTeS QDs.

Organometallic hot-injection synthesis of quaternary-alloyed CdSeTeS QDs was carried out according to our previously reported method using CdO, Se, S as the basic precursors.(Adegoke et al., 2015)

1.2 Synthesis of QD@MHS NPs.

For the synthesis of hollow Fe_2O_3 shell around the CdSeTeS fluorescent core, 54 mg of CdSeTeS nanoparticles were dispersed in a mixture of 10 mL 1-octadecene and 0.05 mL oleylamine with brief sonication. The solution was degassed under vacuum at 120 °C for 30 min, followed by heating to 180 °C under Ar gas. When the solution reached the desired temperature, 0.1 mL of $Fe(CO)_5$ in 1 mL 1-octadecene was injected to the solution which was kept at 180 °C for 30 min. This step resulted with metallic Fe shell around the CdSeTeS core. The solution was cooled to 100 °C, at which point controlled oxidation of the iron was achieved with O_2/Ar mixture. This resulted with formation of hollow Fe_2O_3 shell encapsulating the CdSeTeS QDs. The magnetic nature of the overall structure was evident immediately after its production and was utilized for cleaning the nanoparticles with a strong magnet. Alternatively, typical washing with toluene and ethanol may purify the produced nanoparticles.

1.3 Surface Modification of QD@MHS NPs.

A literature reported method was followed for the ligand exchange reaction with minor modifications.(Korpany et al., 2013) The QD@MHS NPs were dispersed in 500 μL

trichloromethane and an equal volume of water was added. Then, 400 μL of solution consisting of MPA and NaOH (pH∼5) was gradually added with ultrasonicating until the QD@MHS NPs were transferred into the inverse phase. After the trichloromethane layer was discarded, the particles were separated by magnetic separation, and washed with absolute ethyl alcohol three times. The residue of the absolute ethyl alcohol was removed using nitrogen.

The MPA-capped QD@MHS NPs were then modified by methoxy polyethylene glycol thiol (mPEG-SH). The nanoparticles were dissolved in 500 μL water containing 1 mM mPEG-SH, and then the pH was adjusted to 8.0 using appropriate amount of NaOH (1 M). This mixture was gently mixed for 30 min at room temperature and then 500 μL of water was added. The molar ratio of the exchange ligand to QD@MHS surface Fe atoms was set roughly at ∼300 molar ratio. Redispersion of the QD@MHS and then magnetic separation yielded a clear solution.

1.4 Characterizations of Synthesized Nanoparticles.

Transmission electron microscopy (TEM), dynamic light scattering (DLS), X-ray diffraction (XRD) patterns, X-ray photoelectron spectroscopy (XPS), UV/Vis absorption spectra, fluorescence and electrochemical impedance measurements were done using the apparatus described in our previous works (Chowdhury et al., 2019; Khoris et al., 2019; Nasrin et al., 2018).

1.5 Preparation of Antibody-conjugated QD@MHS NPs.

For antibody-conjugated CdSeTeS-QD@Fe_2O_3 hollow sphere (QD@MHS-Ab), EDC/NHS chemistry was adopted (Ganganboina and Doong 2019; Ganganboina et al., 2017).

In brief, 5.1 μg of antibody solution was mixed with 0.1 M EDC in phosphate-buffer saline (PBS), to create an active-ester intermediate on the carboxyl group of the antibody. Further, 1 mL of QD@MHS NPs were mixed with 0.1 M NHS and stirred continuously at 7 °C for 16 h, enabling the amine reaction among the amino group and nanoparticles surface. Unreacted EDC and NHS were removed by magnetically separating the nanoparticles. The prepared QD@MHS-Ab solution in 0.1 M (PBS, pH 7.4) was stored at 4 °C for further use.

1.6 Preparation of biological samples.

The G3 HEV-LPs were produced by a recombinant baculovirus expression system as described previously (Chowdhury et al. 2019). NoV-LPs were expressed in *Trichoplusia ni*, BTL-Tn 5B1-4 (Tn5) by transfection of recombinant baculovirus TCN-VP1 (Invitrogen, San Diego, CA, USA). Thus expressed NoV-LPs were purified and then quantified in accordance to the standard method for virus-like particle (VLP) preparation (Ahmed et al., 2017). HEVs/G7 were obtained from cell culture supernatant of a cell line of human hepatocarcinoma, PLC/PRF/5 (JCRB0406, the Health Science Research Resources Bank, Osaka, Japan) (Li et al., 2016). The RNA copy numbers of HEVs were 5.0×10^8 RNA copies mL^{-1}. NoV was obtained from clinical feces samples collected from infected patients with infectious gastroenteritis, including foodborne illness, as determined by inspections based on laws and ordinances. One hundred μg of fecal sample was added to 900 μL of PBS, (pH 7.4), solids were separated, and the supernatant was used for the detection sample. The NoV concentration of these supernatants was evaluated to be GⅡ.3: 7.2×10^8 RNA copies mL^{-1}, by RT-PCR.

The anti-HEV IgG antibody obtained from a rabbit 136 which were immunized with purified G3 HEV-LPs and purified by protein G column. Anti-NoV antibody which is widely reactive to genogroup II (Monoclonal antibody NS14) was utilized. NS14 (isotype - IgG) was

acquired from spleen cells of mice immunized orally. Thus obtained antibody was purified by protein G and the concentration is 0.3 mg mL^{-1} (Li et al., 2011).

Zika virus (ZIKV) strain PRVABC-59 was provided by Professor Kouichi Morita (Institute of Tropical Medicine, Nagasaki University, Japan).

Anti-WSSV VP28 antibody [ab26935] and a mouse monoclonal antibody [B219M] were purchased from Abcam Inc. (Cambridge, UK). Anti-HA antibody (New Caledonia/20/99) (H1N1) was purchased from Prospec-Tany Techno Gene Ltd. (Rehovot, Israel).

1.7 Fabrication of Reduced Graphene Oxide (rGO)-coated gold electrode and antibody binding.

Gold working electrode was ultrasonically washed with ultrapure water, ethanol, and ultrapure water. After being washed, rGO was introduced to the Au surface by immersing the Au working electrodes into the 1 mg mL^{-1} GO solution using cyclic voltammetry (CV) with a scan range from 0 to −1.5 V and a scan rate of 50 mV s^{-1}. Subsequently, desired antibodies were easily bound with Au||rGO electrode using EDC/NHS covalent chemistry as described earlier for conjugating the antibodies with QD@MHS NPs.

Table S1. Electrochemically fitted parameters of Au||rGO/Anti-HEV electrode obtained from impedance analysis based upon the proposed equivalent circuit after incubating with different concentration of HEV-LPs.

HEV-LPs	R_s (Ω)	n	W (mΩ)	R_{ct} (Ω)
0	285	0.65	0.018	1800
10 fg mL^{-1}	344	0.822	0.011	9402
100 fg mL^{-1}	354	0.818	0.081	12871
1 pg mL^{-1}	358	0.854	0.076	15685
10 pg mL^{-1}	362	0.884	0.038	19975
100 pg mL^{-1}	352	0.847	0.056	24500
1 ng mL^{-1}	339	0.881	0.018	29446
10 ng mL^{-1}	352	0.981	0.021	35268

Table S2. Comparison of the dual-modality VONP-LPs/MNP biosensor with recently reported methods in respect to linear range and detection limit.

Target virus	Sensing method	Linear range	LOD	Ref
Norovirus RNA	Fluorometric	2–18 copies mL^{-1}	1.2 copies mL^{-1}	(Huang et al., 2018)
NoV-LP and Clinical NoV	Colorimetric	10^2–10^6 copies mL^{-1}	13.2 copies mL^{-1}	(Khoris et al. 2019)
Influenza virus	Fluorometric	$1^{-10} \times 10^{-11}$ g mL^{-1}	3×10^{-10} g mL^{-1}	(Takemura et al., 2017)
Influenza A virus	Colorimetric	5×10^{-15} – 5×10^{-6} g mL^{-1}	44.2×10^{-15} g mL^{-1}	(Oh et al., 2018)
Dengue RNA	Fluorometric	5–500 $\times 10^{-9}$ g mL^{-1}	5.2×10^{-9} g mL^{-1}	(Linares et al., 2013)
HBV	Fluorometric	>264 $\times 10^{-9}$ g mL^{-1}	8.3×10^{-9} g mL^{-1}	(Zeng et al., 2012)
HEV RNA	RT-qPCR	10–10^9 copies mL^{-1}	10 copies mL^{-1}	(Jothikumar et al., 2006)
HEV	Impedance	10^{-12} –10^{-15} g mL^{-1}	8×10^{-14} g mL^{-1}	(Chowdhury et al. 2019)
HEV-LP	Fluorometric	10 fg mL^{-1} – 10 ng mL^{-1}	2.6 fg mL^{-1}	This work
HEV RNA	Impedance	10^2–10^7 copies mL^{-1}	57 copies mL^{-1}	This work

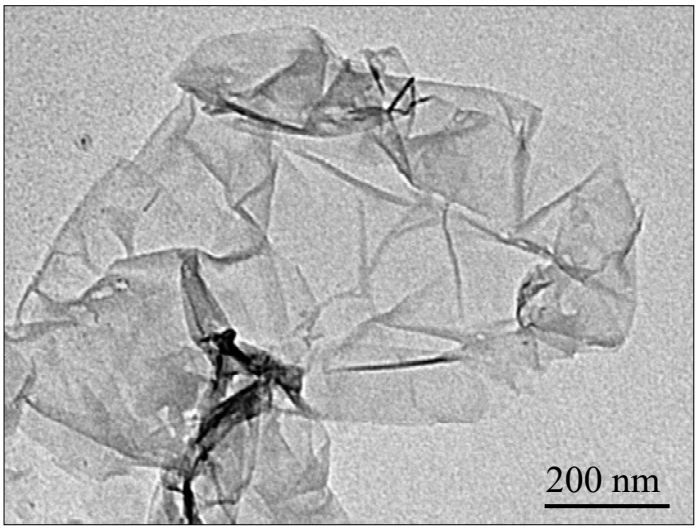

Fig. S1. TEM image of reduced graphene oxide (rGO) sheet.

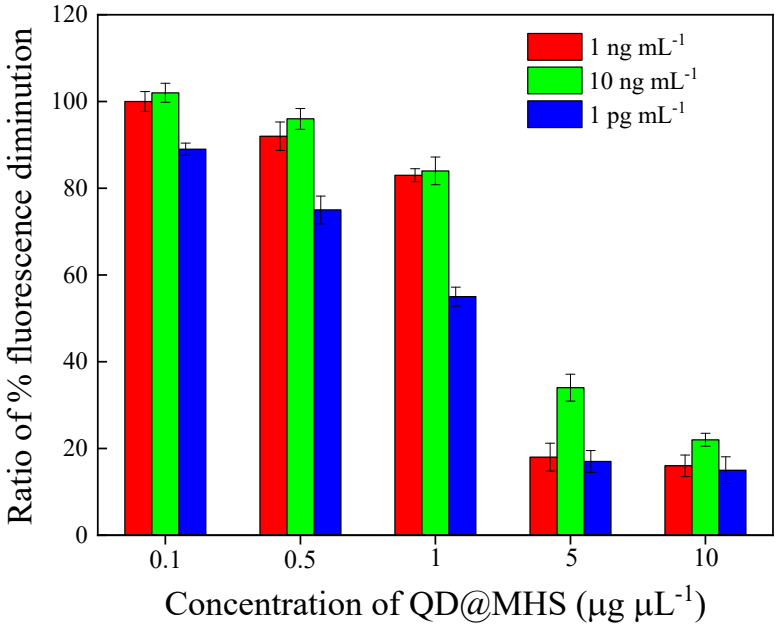

Fig. S2. Optimization of QD@MHS NPs concentration on fluorescence intensity in the presence of 1 ng mL^{-1}, 10 ng mL^{-1}, and 1 pg mL^{-1} HEV-LPs.

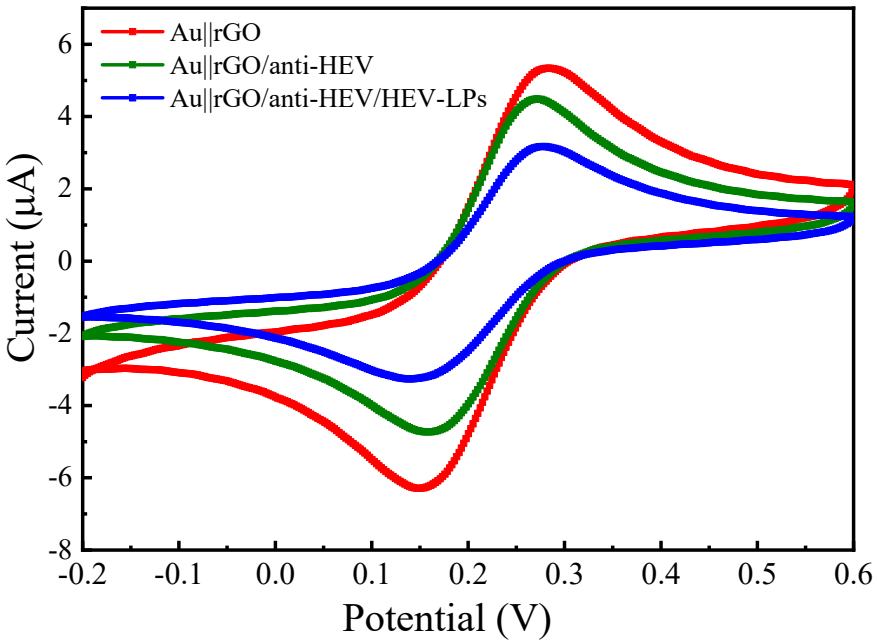

Fig. S3. The cyclic voltammograms of Au||rGO electrode modified with Anti-HEV and HEV-LPs.

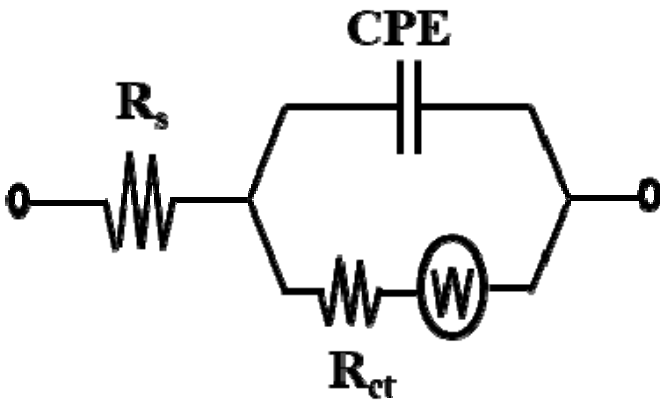

Fig. S4. Equivalent circuit diagram of the proposed sensor.

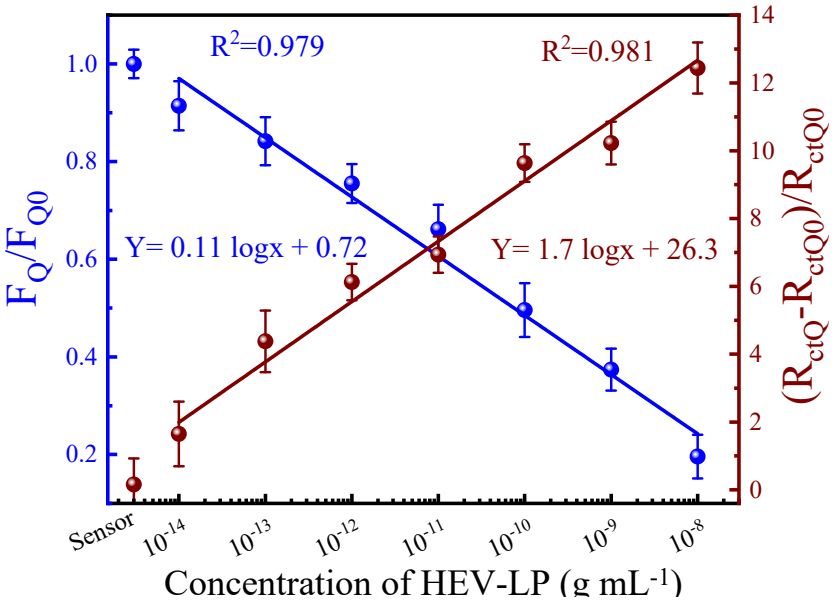

Fig. S5. Detection of HEV-LPs in human serum spiked samples. The dual-modality calibration curve, change of fluorescence intensity of QD@MHS NPs and charge transfer resistance of Au||rGO/antibody electrode vs. concentration of HEV-LPs

References

Adegoke, O., Nyokong, T., Forbes, P.B., 2015. J. Alloys Compd. 645, 443–449.

Ahmed, S.R., Takemeura, K., Li, T.-C., Kitamoto, N., Tanaka, T., Suzuki, T., Park, E.Y., 2017. Biosens. Bioelectron. 87, 558–565.

Chowdhury, A.D., Takemura, K., Li, T.-C., Suzuki, T., Park, E.Y., 2019. Nature Comm. 10, 3737.

Ganganboina, A.B., Doong, R.-A., 2019. Scientific reports 9, 7214.

Ganganboina, A.B., Dutta Chowdhury, A., Doong, R.-a., 2017. ACS Sustainable Chem. Eng. 5(6), 4930–4940.

Huang, Z.-H., Song, Y., Feng, D.-Y., Sun, Z., Sun, X., Liu, X.-X., 2018. ACS Nano 12(4), 3557–3567.

Jothikumar, N., Cromeans, T.L., Robertson, B.H., Meng, X., Hill, V.R., 2006. J. Virol. Methods 131(1), 65–71.

Khoris, I.M., Takemura, K., Lee, J., Hara, T., Abe, F., Suzuki, T., Park, E.Y., 2019. Biosens. Bioelectron. 126, 425–432.

Korpany, K.V., Habib, F., Murugesu, M., Blum, A.S., 2013. Mater. Chem. Phys. 138(1), 29–37.

Li, T.-C., Yoshimatsu, K., Yasuda, S.P., Arikawa, J., Koma, T., Kataoka, M., Ami, Y., Suzaki, Y., Mai, L.T.Q., Hoa, N.T., 2011. J. Gen. Virol. 92(12), 2830.

Li, T.-C., Zhou, X., Yoshizaki, S., Ami, Y., Suzaki, Y., Nakamura, T., Takeda, N., Wakita, T., 2016. J. Hepatol. 65(6), 1104–1111.

Linares, E.M., Pannuti, C.S., Kubota, L.T., Thalhammer, S., 2013. Biosens. Bioelectron. 41, 180-185.

Nasrin, F., Chowdhury, A.D., Takemura, K., Lee, J., Adegoke, O., Deo, V.K., Abe, F., Suzuki, T., Park, E.Y., 2018. Biosens. Bioelectron. 122, 16–24.

Oh, S., Kim, J., Tran, V.T., Lee, D.K., Ahmed, S.R., Hong, J.C., Lee, J., Park, E.Y., Lee, J., 2018. ACS Appl. Mater. Interfaces 10(15), 12534–12543.

Takemura, K., Adegoke, O., Takahashi, N., Kato, T., Li, T.-C., Kitamoto, N., Tanaka, T., Suzuki, T., Park, E.Y., 2017. Biosens. Bioelectron. 89, 998–1005.

Zeng, Q., Zhang, Y., Liu, X., Tu, L., Kong, X., Zhang, H., 2012. Chem. Comm. 48(12), 1781–1783.